

Role of Hund's splitting in electronic phase competition in $\text{Pb}_{1-x}\text{Sn}_x\text{Te}$

S.Kundu and V.Tripathi

*Department of Theoretical Physics, Tata Institute of Fundamental Research,
Homi Bhabha Road, Navy Nagar, Colaba, Mumbai-400005*

(Dated: June 16, 2021)

We study the effect of Hund's splitting of repulsive interactions on electronic phase transitions in the multiorbital topological crystalline insulator $\text{Pb}_{1-x}\text{Sn}_x\text{Te}$, when the chemical potential is tuned to the vicinity of low-lying Type-II Van Hove singularities. Nontrivial Berry phases associated with the Bloch states impart momentum-dependence to electron interactions in the relevant band. We use a multipatch parquet renormalization group (RG) analysis for studying the competition of different electronic phases, and find that if the dominant fixed-point interactions correspond to antiparallel spin configurations, then a chiral p -wave Fulde-Ferrell-Larkin-Ovchinnikov (FFLO) state is favored, otherwise, none of the commonly encountered electronic instabilities occur within the one-loop parquet RG approach.

Topological crystalline insulators (TCIs) have low-energy surface states in certain high symmetry directions, protected by crystalline symmetry [1]. Unlike conventional Z_2 topological insulators [2–5], the nature of these low-energy states is sensitive to the surface orientation. In particular, it has been shown in the recently discovered TCI $\text{Pb}_{1-x}\text{Sn}_x\text{Te}$ [6–9] that the band structure of the (001) surface allows for the presence of Type-II Van Hove singularities [10], with a diverging density of states, which opens up the possibility of a variety of competing Fermi-surface instabilities brought about by weak repulsive interparticle interactions [11–15]. In particular, the parquet approximation for studying competing phases in a system with multiple Fermi pockets has proved very useful in the context of unconventional superconductivity [16–18] in cuprates [19], graphene [20] and semimetal thin films [21]. However, in a multiorbital system like $\text{Pb}_{1-x}\text{Sn}_x\text{Te}$, phase competition needs to be studied taking into account the effect of Hund's splitting of interactions. The importance of Hund's coupling has generally been underemphasized in parquet renormalization group analyses of multiorbital systems for reasons of convenience, but recent developments show that Hund's coupling may play an important role in electronic instabilities of multiorbital systems [22, 23].

In this paper, we employ a multipatch parquet renormalization group (RG) analysis including Hund's splitting effects, and show that even relatively small amounts of Hund's splitting can have a dramatic effect on the very existence of electronic instabilities on the surface of $\text{Pb}_{1-x}\text{Sn}_x\text{Te}$. Depending on the sign of the Hund's splitting, we find that away from perfect nesting, either a chiral p -wave FFLO [24, 25] state is stabilized or none of the commonly encountered electronic instabilities occur at the level of the one-loop parquet approach. A characteristic feature of $\text{Pb}_{1-x}\text{Sn}_x\text{Te}$ is that the surface bands are effectively spinless, which rules out s -wave pairing, that would otherwise prevail over p -wave pairing in the presence of nonmagnetic disorder [26–28].

The topological crystalline insulator surface that we

consider offers certain natural advantages from an experimental point of view. It provides two-dimensional Van Hove singularities which are accessible through a small change in doping, unlike, say, graphene, where a very high level of doping is required. Interestingly, as we show below, the p -wave symmetry originates not from intrinsic Fermi surface deformations, but from the nontrivial Berry phases associated with the topological states. This is reminiscent of chiral p -wave superconductivity enabled by a topological Berry phase in fermionic cold atom systems with attractive momentum-independent interactions [29]. We argue that the p -wave superconductivity on the TCI surface is more robust against potential disorder [30, 31] than in, say, Sr_2RuO_4 [32]. Moreover, the p -wave superconductivity here is intrinsic, unlike proximity-induced p -wave superconductivity on topological insulator surfaces where recently Majorana fermions have been detected [33]. Finally, such an FFLO state in a pure solid state system in the absence of an applied magnetic field is a rather unusual occurrence (see, e.g. Refs [34] and [35]). Ref. [36] also discusses an intranode FFLO pairing in a doped Weyl semimetal, although the stability of such a state in this system is still a controversial issue [37–39].

The band gap minima of IV-VI semiconductors are located at the four L points in the FCC Brillouin zone. In [40], the TCI surface states are classified into two types: *Type-I*, for which all four L -points are projected to the different time-reversal invariant momenta (TRIM) in the surface Brillouin zone, and *Type-II*, for which different L -points are projected to the same surface momentum. The (001) surface falls into the latter class of surfaces, for which the L_1 and L_2 points are projected to the \bar{X}_1 point on the surface, and the L_3 and L_4 points are projected to the symmetry-related \bar{X}_2 point. This leads to two co-existing massless Dirac fermions at \bar{X}_1 arising from the L_1 and the L_2 valley, respectively, and likewise at \bar{X}_2 . The k.p Hamiltonian close to the point \bar{X}_1 on the (001) surface is derived on the basis of a symmetry analysis in

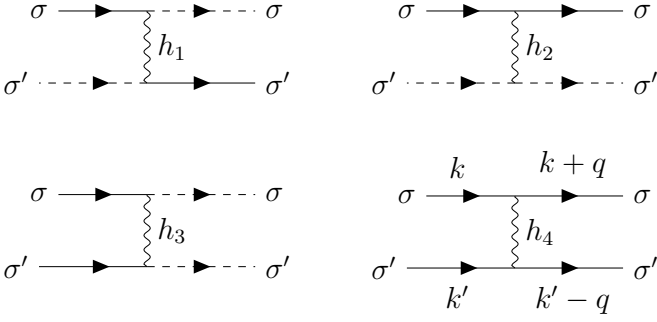


Figure 1. The different types of Coulomb interaction processes in our low-energy model (Eq.3). The solid lines and dashed lines denote two different patches \bar{X}_1 and \bar{X}_2 in momentum space, on the (001) surface. All the vertices have momentum-dependences as indicated for h_4 . The σ 's refer to the particular spin components of the (spinor) wavefunctions associated with the bands under consideration (see text for more details).

[40], and is given by

$$H_{\bar{X}_1}(k) = (v_x k_x s_y - v_y k_y s_x) + m\tau_x + \delta s_x \tau_y, \quad (1)$$

where k is measured with respect to \bar{X}_1 , \vec{s} is a set of Pauli matrices associated with the two spin components associated with each valley, τ operates in valley space, and the terms m and δ , which are off-diagonal in valley space, are added to describe intervalley scattering. The band dispersion and constant energy contours for the above surface Hamiltonian undergo a Lifshitz transition with increasing energy away from the Dirac point, and when the Fermi surface is at $\delta = 26$ meV (as taken from [40]) two saddle points \bar{S}_1 and \bar{S}_2 at momenta $(\pm \frac{m}{v_x}, 0)$ lead to a Van-Hove singularity in the density of states. A similar situation arises at the point \bar{X}_2 .

In addition to the noninteracting part of the Hamiltonian described in Eq.1 above, we now consider interactions between surface electrons corresponding to different valleys and spins, which gives rise to the following terms in the Hamiltonian-

$$H_I = \frac{1}{2} \sum_{a,b,c,d,\sigma,\sigma'} U_{abcd}^{\sigma\sigma'} c_{a\sigma}^\dagger c_{b\sigma'}^\dagger c_{c\sigma'} c_{d\sigma} \quad (2)$$

where a, b, c, d refer to different valleys (which are either all the same, same in pairs or all different in the above sum) and σ, σ' refer to spins. Here, we consider $U_{abcd}^{\sigma\sigma'} = U_1^{\sigma\sigma'}$ when (a, c) belong to one \bar{X} -point (i.e. the L-valleys corresponding to (a, c) are projected to one of the \bar{X} -points) and (b, d) belong to the other \bar{X} -point. Similarly, $U_{abcd}^{\sigma\sigma'} = U_2^{\sigma\sigma'}$ when (b, c) belong to one \bar{X} -point and (a, d) belong to the other, $U_3^{\sigma\sigma'}$ when (a, b) belong to one \bar{X} -point and (c, d) to the other, and $U_4^{\sigma\sigma'}$ when a, b, c and d all correspond to L-points projected to the same \bar{X} -point. The interactions depend only on the relative orientations of the spins, for example, $U^{\sigma\sigma'}$ can be written as $U^{\sigma\sigma} \delta_{\sigma\sigma'} + U^{\sigma\bar{\sigma}} (1 - \delta_{\sigma\sigma'})$. In our analysis, we have

projected the interactions between electrons in the valley-spin picture to the positive-energy band lying closest to the Van-Hove singularities [41]. The resulting multiplicative form factors $u_{\sigma ai}$ (for a transformation from valley a , spin σ to the i th band) lend a momentum dependence to the effective pairing interactions obtained upon projection. We find that the spin \uparrow components of the form factors have an $\exp[i\theta_k]$ dependence in momentum space and transform as $\ell = 1$ objects, whereas the phase of the spin \downarrow components remains unchanged upon advancing by an angle of 2π around the \bar{X}_r ($r = 1, 2$) points, and these show an $\ell = 0$ angular dependence. These additional phase factors arise from the Berry phases associated with the surface states of the crystalline topological insulator. After projecting to the two bands intersecting with the Fermi level, we obtain the following low-energy theory

$$\begin{aligned} L = & \sum_i \psi_i^\dagger (\partial_\tau - \epsilon_k + \mu) \psi_i - \sum_{i,\sigma,\sigma'} \frac{1}{2} h_4^{\sigma\sigma'} \psi_i^\dagger \psi_i^\dagger \psi_i \psi_i \\ & - \sum_{i \neq j, \sigma, \sigma'} \frac{1}{2} (h_1^{\sigma\sigma'} \psi_i^\dagger \psi_j^\dagger \psi_i \psi_j + h_2^{\sigma\sigma'} \psi_i^\dagger \psi_j^\dagger \psi_j \psi_i \\ & + h_3^{\sigma\sigma'} \psi_i^\dagger \psi_i^\dagger \psi_j \psi_j) \\ = & \sum_i \psi_i^\dagger (\partial_\tau - \epsilon_k + \mu) \psi_i - (h_4^0 + h_4^1) \psi_i^\dagger \psi_i^\dagger \psi_i \psi_i \\ & - \sum_{i \neq j} ((h_1^0 + h_1^1) \psi_i^\dagger \psi_j^\dagger \psi_i \psi_j + (h_2^0 + h_2^1) \psi_i^\dagger \psi_j^\dagger \psi_j \psi_i \\ & + (h_3^0 + h_3^1) \psi_i^\dagger \psi_i^\dagger \psi_j \psi_j) \end{aligned} \quad (3)$$

with $h_r^0 = \frac{1}{2} \sum_\sigma h_r^{\sigma\sigma}$ and $h_r^1 = \frac{1}{2} \sum_\sigma h_r^{\sigma\bar{\sigma}}$ where the quadratic noninteracting part comes from the model in Eq.1. The chemical potential value $\mu=0$ corresponds to the system being doped to the Van Hove singularities. Here h_4 refers to different scattering processes within a band i , whereas h_1, h_2 and h_3 refer to exchange processes, Coulomb interactions and pair hopping between electrons corresponding to the two different bands under consideration (see Fig. 1). Due to the distinct phase dependences associated with the form factors corresponding to spins \uparrow and \downarrow , the effective interactions h_r after projection to the low-energy bands also either have a phase factor of $\exp[i(\theta_k - \theta_{k'})]$ (for spin-antiparallel configurations) and behave as $\ell = 1$ objects, or have no additional phase factors (for spin-parallel configurations) and behave as $\ell = 0$ objects. The coupling constants $h_r^0 \propto h_r^{\sigma\sigma}$ and $h_r^1 \propto h_r^{\sigma\bar{\sigma}}$ respectively correspond to $\ell = 0$ and $\ell = 1$ angular momentum components of the interaction in our simplified model in Eq.3 above. It is important to note that although the surface bands are effectively spinless, we associate spin indices $\sigma\sigma'$ (or equivalently the superscripts 0 and 1) with the interactions h_r in the different scattering channels r , due to the phase dependences associated with interactions between electrons with different spin configurations. In doing so, we allow for the

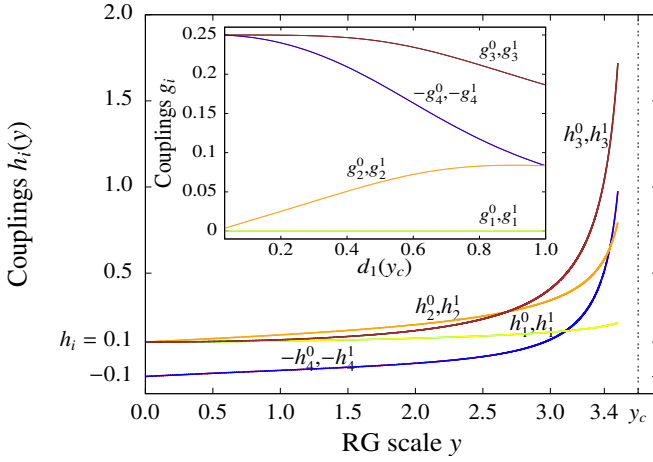


Figure 2. Flow of couplings with renormalization group scale y , starting with repulsive interactions, where the couplings in different angular momentum channels (h_r^0 and h_r^1) are assumed to be degenerate initially, at $(h_r^{0,1})_{\text{initial}} = 0.1$. We find pair hopping between patches (h_3) and on-patch scattering (h_4) to be the dominant scattering channels. Here, the critical point $y_c \approx 3.65$.

The inset shows the evolution of the fixed-point couplings g_r^ℓ ($\ell = 0, 1$) as a function of $d_1(y_c) (= \frac{1}{\sqrt{1+y_c}})$, which is the ratio of the particle-hole to particle-particle susceptibilities at the fixed point y_c .

Coulomb interactions between electrons to depend on the spin configuration being considered, thereby incorporating the effects of Hund's splitting of interactions in our treatment.

To study the possible instabilities in this system, we construct a two-patch renormalization group for the interaction vertices. In the RG analysis, the instability is indicated in the form of a pole in the vertex function. We consider only the electrons near the saddle points at $\overline{X_1}$ and $\overline{X_2}$ on the (001) surface. In our RG analysis, we distinguish between coupling constants with different spin combinations ($h_r^{\sigma\sigma}$ and $h_r^{\sigma\bar{\sigma}}$, or equivalently h_r^0 and h_r^1 respectively) and write separate RG equations for the two kinds of interactions.

We perform RG analysis up to one-loop level, integrating out high-energy degrees of freedom gradually from an energy cutoff Λ , which is the bandwidth. The susceptibilities in the different channels schematically behave as $\chi_0^{pp}(\omega) \sim \ln[\Lambda/\omega] \ln[\Lambda/\max(\omega, \mu)]$, $\chi_Q^{ph}(\omega) \sim \ln[\Lambda/\max(\omega, \mu)] \ln[\Lambda/\max(\omega, \mu, t)]$ and $\chi_0^{ph}(\omega), \chi_Q^{pp}(\omega) \sim \ln[\Lambda/\max(\omega, \mu)]$, where ω denotes the energy away from the Van Hove singularities and t represents terms in the Hamiltonian that destroy the perfect nesting.

We use $y \equiv \ln^2[\Lambda/\omega] \sim \chi_0^{pp}$ as the RG flow parameter, and describe the relative weight of the other channels as $d_1(y) = \frac{d\chi_Q^{ph}}{dy}$, $d_2(y) = \frac{d\chi_0^{ph}}{dy}$ and $d_3(y) = -\frac{d\chi_Q^{pp}}{dy}$, where $d_1(y)$ is taken to be a function $\frac{1}{\sqrt{1+y}}$ [20], interpolating smoothly in between the limits $d_1(y=0) = 1$

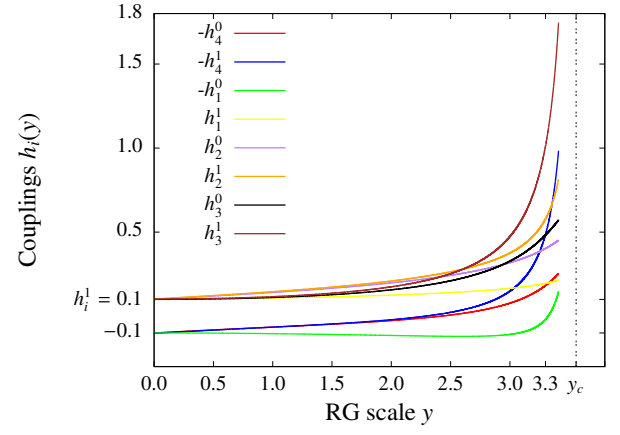


Figure 3. Flow of couplings with renormalization group scale y , starting with repulsive interactions, where the $\ell = 1$ components of all the couplings are chosen to be larger than the $\ell = 0$ components by 2% initially, i.e. $\frac{|h_r^1 - h_r^0|}{|h_r^0|} = 0.02$, where $(h_r^0)_{\text{initial}} = 0.1$. We find the $\ell = 1$ components of pair hopping between patches (h_3) and on-patch scattering (h_4) to be the most dominant couplings in this case. Here, the critical point $y_c \approx 3.56$.

and $d_1(y \gg 1) = \frac{1}{\sqrt{y}}$, and $d_2, d_3 \ll d_1$. The multiplicative factor $d_1(y)$ essentially incorporates the effects of imperfect nesting in our analysis. The RG equations are obtained by evaluating second-order diagrams and collecting the respective combinatoric prefactors, for each of the interactions h_1, h_2, h_3 and h_4 . The diagrams corresponding to the renormalization of the interaction h_2 are shown in Fig. 7 in the Supplementary as an illustrative example. The RG equations obtained are given by (where we have used the notation $\sigma\sigma \equiv 0$ and $\sigma\bar{\sigma} \equiv 1$ for each of the couplings)

$$\begin{aligned} \frac{dh_1^0}{dy} &= 2d_1(-(h_1^0)^2 - (h_3^1)^2 - (h_1^1)^2 \\ &\quad + 2h_1^0 h_2^0 + (h_3^0)^2), \end{aligned} \quad (4)$$

$$\frac{dh_1^1}{dy} = 2d_1(-2h_1^0 h_1^1 + 2h_1^1 h_2^0), \quad (5)$$

$$\frac{dh_2^0}{dy} = 2d_1((h_2^0)^2 + (h_3^0)^2), \quad (6)$$

$$\frac{dh_2^1}{dy} = 2d_1((h_2^1)^2 + (h_3^1)^2), \quad (7)$$

$$\frac{dh_3^0}{dy} = -4h_4^0h_3^0 + 2d_1(4h_2^0h_3^0 - 2h_1^1h_3^1), \quad (8)$$

$$\frac{dh_3^1}{dy} = -4h_4^1h_3^1 + 2d_1(2h_2^1h_3^1 - 2h_1^0h_3^1 + 2h_2^0h_3^1), \quad (9)$$

$$\frac{dh_4^0}{dy} = -2((h_4^0)^2 + (h_3^0)^2), \quad (10)$$

$$\frac{dh_4^1}{dy} = -2((h_4^1)^2 + (h_3^1)^2). \quad (11)$$

These coupled differential equations are then solved, starting from initial values of interactions in the weak-coupling regime ($h_r^0 = h_r^1 \sim 0.1$). The results for the cases where (a) the couplings h_r^ℓ are degenerate for $\ell = 0$ and $\ell = 1$, (b) the couplings h_r^ℓ in the $\ell = 1$ channel are chosen to dominate initially, (c) the couplings h_r^ℓ in the $\ell = 0$ channel are chosen to dominate initially, are shown in the Figures 2,3 and 4 respectively. The figures show results for a Hund's splitting of 2%, and we have verified that even for a splitting of 0.1% introduced initially between the interactions in the $\ell = 0$ and $\ell = 1$ channels ($\frac{|h_r^1 - h_r^0|}{|h_r^1 + h_r^0|} \sim 0.1\%$) the final set of dominant couplings g_r^ℓ near the critical point of the RG correspond to the value of ℓ which has been chosen to dominate initially. Thus, the results of our RG analysis are found to be extremely sensitive to the sign of the Hund's splitting. In contrast, the results are remarkably insensitive to the magnitude as well as sign of an initial splitting introduced between the couplings h_r corresponding to the different scattering channels $r = 1 - 4$. This is graphically depicted in Fig.10 in the Supplementary.

We now investigate the instabilities of the system by evaluating the susceptibilities χ for various types of order, introducing infinitesimal test vertices corresponding to different kinds of pairing into the action, such as $\Delta_a \psi_{a\sigma}^\dagger \psi_{a\sigma'}^\dagger + \Delta_a^* \psi_{a\sigma} \psi_{a\sigma'}$ for the patch $a = 1, 2$ (where the spin labels σ, σ' are meant to simply denote the presence or absence of the phase factors $\exp[i\theta_k]$) corresponding to particle-particle pairing on the patch [20].

The renormalization of the test vertex for particle-particle pairing on a patch is governed by the equation [20]

$$\frac{\partial}{\partial y} \begin{pmatrix} \Delta_1 \\ \Delta_2 \end{pmatrix} = 2 \begin{pmatrix} h_4^1 & h_3^1 \\ h_3^1 & h_4^1 \end{pmatrix} \begin{pmatrix} \Delta_1 \\ \Delta_2 \end{pmatrix} \quad (12)$$

since we can only consider Cooper pairing in the p -wave channel for spinless electrons. By transforming to the eigenvector basis, we can obtain different possible order parameters, and choose the one corresponding to the most negative eigenvalue. The vertices with positive eigenvalues are suppressed under RG flow.

At an electronic instability, the most divergent susceptibility χ determines the nature of the ordered phase.

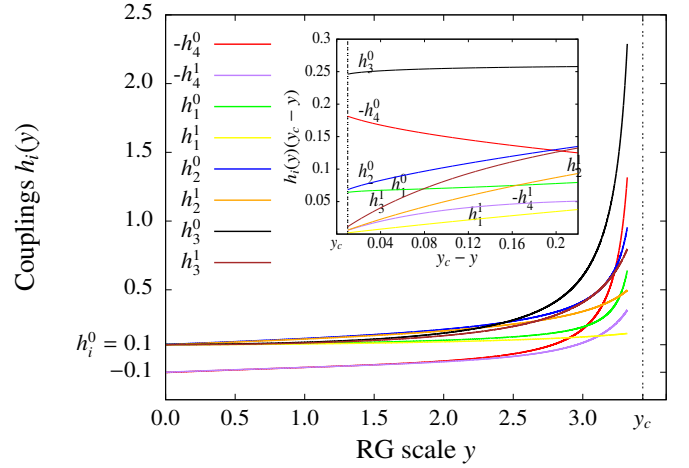


Figure 4. Flow of couplings with renormalization group scale y , starting with repulsive interactions, where the $\ell = 0$ components of all the couplings are chosen to be larger than the $\ell = 1$ components by 2% initially, i.e. $\frac{|h_r^0 - h_r^1|}{|h_r^1|} = 0.02$, where $(h_r^1)_{\text{initial}} = 0.1$. We find the $\ell = 0$ components of pair hopping between patches (h_3) and on-patch scattering (h_4) to be the most dominant couplings in this case. Here, the critical point $y_c \approx 3.4$.

The inset shows the behavior of $h_r(y)(y_c - y)$ as a function of $(y_c - y)$ close to the fixed point y_c . The y -intercepts of the different curves show the fixed-point values g_r^ℓ for the couplings $h_r^\ell(y)$. Evidently, the dominant couplings near the critical point correspond to the $\ell = 0$ channel in this case.

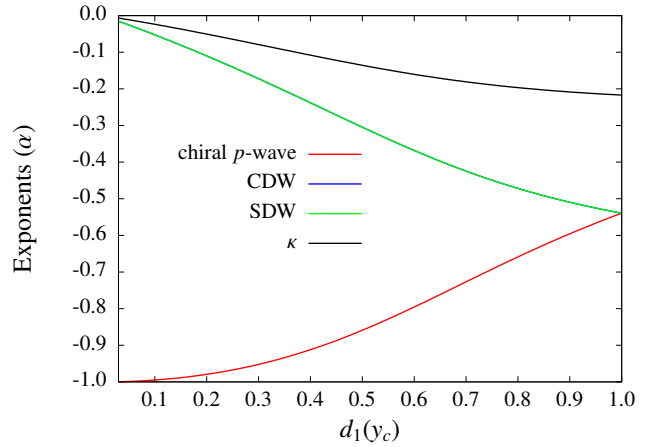


Figure 5. The exponents α , which are negative, corresponding to the various susceptibilities: chiral p -wave superconductivity, CDW, SDW and uniform charge compressibility (κ), plotted as a function of $d_1(y_c)$ for the case where each of the couplings g_r^ℓ for $r = 1 - 4$ and $\ell = 0, 1$ are degenerate. The order of these exponents indicates that chiral p -wave superconductivity is the leading instability (with the most negative exponent α_{pw}) throughout, and CDW and SDW have nearly the same values of exponents α in this case.

Each of the couplings associated with the RG flow has an asymptotic form $h_r^\ell(y) = \frac{g_r^\ell}{y_c - y}$ near the instability threshold. The coefficients g_r^ℓ can be determined as a function of $d_1(y_c)$ (the results for the case, where we start with identical initial values for each of the couplings, are shown in the inset in Fig. 2). We diagonalize the Eq. 12 above and substitute the asymptotic form of the interactions in the most negative eigenvalue. This gives us the exponent α for the divergence of the susceptibility $\chi \propto (y_c - y)^\alpha$ for p -wave superconductivity. Likewise we can introduce test vertices for other possible instabilities and obtain the corresponding exponents for their susceptibilities [41]. The exponents for intrapatch p -wave pairing, charge-density wave, spin-density wave, uniform spin, charge compressibility (κ) and finite-momentum π pairing are given by-

$$\begin{aligned}\alpha_{\text{pw}} &= 2(-g_3^1 + g_4^1), \\ \alpha_{\text{CDW}} &= -2(g_3^1 - g_1^0 - g_1^1 + g_2^0)d_1(y_c), \\ \alpha_{\text{SDW}} &= -2(g_3^1 + g_2^1)d_1(y_c), \\ \alpha_\kappa &= -2(-g_4^1 - (g_1^0 - g_2^0 - g_2^1))d_2(y_c), \\ \alpha_s &= -2(g_4^1 + g_1^1)d_2(y_c), \\ \alpha_\pi^0 &= 2(g_2^0 - g_1^0)d_3(y_c), \\ \alpha_\pi^1 &= 2(g_2^1 - g_1^1)d_3(y_c).\end{aligned}\quad (13)$$

The p -wave order here is chiral since its symmetry is dictated by the aforementioned $\exp[i\theta_k]$ dependence of the Berry phase factors in the wave functions. It is important to note that we have p -wave order on the patches, unlike [10] and [21]. Consequently, this is a finite-momentum pairing, with each patch \bar{X}_i located at a finite momentum with respect to the $\bar{\Gamma}$ point on the surface. Furthermore, the relative phase of the p -wave order on different patches is π , which means that we have d -wave order between the patches [41].

Figure 5 shows the behavior of the exponents for p -wave pairing, SDW, CDW and charge compressibility as a function of $d_1(y_c)$. Comparison between the values of these exponents shows that the most divergent susceptibility is p -wave superconductivity throughout the parameter range $0 < d_1(y_c) < 1$. The CDW and SDW instabilities show a weaker divergence, and are followed by charge compressibility. The exponents for uniform spin susceptibility and π pairing are always positive and hence, these orders are suppressed. In the case of perfect nesting, i.e $d_1 = 1$, the SDW and CDW instabilities become degenerate with p -wave superconductivity.

Now, if a finite Hund's splitting is introduced initially such that $h_r^1 > h_r^0$, the above analysis holds and p -wave superconductivity is still the dominant instability. However, for an initial Hund's splitting of the opposite sign, i.e. $h_r^0 > h_r^1$, we find that the dominant couplings g_r^ℓ at the instability threshold correspond to $\ell = 0$. In this case, the exponents α for each of the susceptibilities χ consid-

ered in Eq.13 turn out to be either positive or numerically close to zero. This is due to subtle cancellations between contributions from the dominant couplings in different scattering channels. Thus, none of the instabilities considered above are found to occur in this case, within the one-loop approximation. Clearly, the nature of instabilities in this system is crucially dependent on the sign of the Hund's splitting.

We now discuss the effects of weak disorder on superconductivity on our crystalline topological insulator surface. Since potential scattering of the electrons changes their momenta, we expect the d -wave pairing across the patches to be sensitive to such disorder. However, within a patch, the p -wave pairing is topologically protected. To see this, note that our order parameter $\langle \psi_k \psi_{-k} \rangle \sim \Delta_0 \exp[i\theta_k]$ (where ψ denotes the spinless fermion in the relevant band and θ_k arises from the nontrivial Berry phases). Translated to the valley-spin picture, this shows that the superconducting order parameter in terms of those fermions has no momentum dependence, and hence, cannot be degraded by weak potential disorder. The p -wave superconductivity is also found to survive in the presence of magnetic impurities for a finite Hund's splitting of interactions [42].

Finally, we discuss the experimental implications of our work. Recently, there have been reports of surface superconductivity induced on the surface of $\text{Pb}_{0.6}\text{Sn}_{0.4}\text{Te}$ by forming a mesoscopic point contact using a nonsuperconducting metal [43]. The observed transition temperature is in the range 3.7-6.5 K. We expect transition temperatures roughly an order of magnitude smaller than the bandwidth Λ , which is of the order of the band gap. However, the nature of the Cooper pair order in the experiment is not yet settled and further experimental work needs to be done in this direction to confirm our prediction of surface p -wave superconductivity in this material. Recently, we have come across a paper [44] which reports the detection of an electron-hole gap with a broad zero-bias conductance maximum at the topological surfaces of diamagnetic, paramagnetic, and ferromagnetic $\text{Pb}_{1-y-x}\text{Sn}_y\text{Mn}_x\text{Te}$ (where $y \gtrsim 0.67$ and $0 \leq x < 0.1$) using soft-contact spectroscopy. The MBS-like conductance spectra obtained with and without magnetic impurities are found to be intrinsic in origin, which we believe supports our claim. Our approach could also be useful for studying phase competition in other two-dimensional systems with multiple Fermi patches in the presence of Hund's splitting. In particular, this could be relevant for Type-II Dirac surface states on certain surfaces of antiperovskites[45], or for the bulk band structure of the Dirac semimetal Na_3Bi with multiple Dirac nodes connecting via a Lifshitz point[46], in a quasi-2D approximation.

The authors gratefully acknowledge useful discussions with Kedar Damle and Rajdeep Sensarma. SK acknowledges Debjyoti Burdhan for his help with some of the fig-

ures. VT acknowledges DST for a Swarnajayanti grant (No. DST/SJF/PSA-0212012-13).

Supplementary material for Role of Hund's splitting in electronic phase competition in $\text{Pb}_{1-x}\text{Sn}_x\text{Te}$:

Here we provide additional information on 1) electron interactions in the valley-spin picture and effective interactions when projected to a band and 2) RG equations for test vertices corresponding to different kinds of pairing, and 3) Fixed point values of different couplings as a function of $d_1(y_c)$

Interactions between electrons in the valley-spin basis:

Here we derive the effective interaction model obtained upon projecting the interactions in the valley-spin basis to one of the surface bands (the positive energy band closest to the saddle points) for each of the \bar{X} points. The interaction Hamiltonian for surface electrons with valley and spin labels is given by

$$H_I = \frac{1}{2} \sum_{a,b,c,d,\sigma,\sigma'} U_{abcd}^{\sigma\sigma'} c_{\sigma a}^\dagger c_{\sigma' b}^\dagger c_{\sigma' c} c_{\sigma d} \quad (14)$$

where a, b, c, d refer to different valleys (which are either all the same, same in pairs or all different in the above sum) and σ, σ' refer to spins. Here, we consider $U_{abcd}^{\sigma\sigma'} = U_1^{\sigma\sigma'}$ when (a, c) belong to one \bar{X} -point (i.e. the L-valleys corresponding to (a, c) are projected to one of the \bar{X} -points) and (b, d) belong to the other \bar{X} -point. Similarly, $U_{abcd}^{\sigma\sigma'} = U_2^{\sigma\sigma'}$ when (b, c) belong to one \bar{X} -point and (a, d) belong to the other, $U_3^{\sigma\sigma'}$ when (a, b) belong to one \bar{X} -point and (c, d) to the other, and $U_4^{\sigma\sigma'}$ when a, b, c and d all correspond to L-points projected to the same \bar{X} -point. The interactions depend only on the relative orientations of the spins, for example, $U^{\sigma\sigma'}$ can be written as $U^{\sigma\sigma} \delta_{\sigma\sigma'} + U^{\sigma\bar{\sigma}} (1 - \delta_{\sigma\sigma'})$. For the k.p Hamiltonian $H_{\bar{X}_1}(k)$ and $H_{\bar{X}_2}(k)$ of the (001) surface, the operators corresponding to different bands can be rewritten in terms of the operators for different valley and spin combinations as follows

$$\begin{aligned} \psi_1 &= A_1 c_{\uparrow 1} + B_1 c_{\downarrow 1} + C_1 c_{\uparrow 2} + D_1 c_{\downarrow 2}, \\ \psi_2 &= A_2 c_{\uparrow 1} + B_2 c_{\downarrow 1} + C_2 c_{\uparrow 2} + D_2 c_{\downarrow 2}, \\ \psi_3 &= A_3 c_{\uparrow 1} + B_3 c_{\downarrow 1} + C_3 c_{\uparrow 2} + D_3 c_{\downarrow 2}, \\ \psi_4 &= A_4 c_{\uparrow 1} + B_4 c_{\downarrow 1} + C_4 c_{\uparrow 2} + D_4 c_{\downarrow 2}, \\ \psi_5 &= A_5 c_{\uparrow 3} + B_5 c_{\downarrow 3} + C_5 c_{\uparrow 4} + D_5 c_{\downarrow 4}, \\ \psi_6 &= A_6 c_{\uparrow 3} + B_6 c_{\downarrow 3} + C_6 c_{\uparrow 4} + D_6 c_{\downarrow 4}, \\ \psi_7 &= A_7 c_{\uparrow 3} + B_7 c_{\downarrow 3} + C_7 c_{\uparrow 4} + D_7 c_{\downarrow 4}, \\ \psi_8 &= A_8 c_{\uparrow 3} + B_8 c_{\downarrow 3} + C_8 c_{\uparrow 4} + D_8 c_{\downarrow 4}, \end{aligned} \quad (15)$$

where $\{A_i, B_i, C_i, D_i, i = 1 \text{ to } 8\}$ correspond to the complex conjugates of the nonzero components of the different normalized energy eigenvectors, and are functions of k_x and k_y in the two-dimensional momentum space. We denote the L-valleys projected to one of the \bar{X} -points by 1 and 2, and those projected to the other point by 3 and 4. Thus, the total number of bands is eight. Since the points \bar{X} are decoupled from each other, four of these components for each eigenvector vanish, giving rise to the expression in Eq. 15. We can invert the above equations to write the $c'_{\alpha a}$ s in terms of ψ'_i s. Substituting all of these expressions into H_I in Eq. 14 above, and writing $c_{\alpha a}$ as $\sum_i u_{\alpha ai} \psi_i$, we have

$$\begin{aligned} H_I &= \frac{1}{2} \left(\sum_{a,b,c,d,\sigma,\sigma'} \sum_{i,j,k,l} U_{abcd}^{\sigma\sigma'} u_{\sigma ai}^* (k'_1) u_{\sigma' bj}^* (k'_2) \right. \\ &\quad \left. \times u_{\sigma' ck} (k_1) u_{\sigma dl} (k_2) \psi_i^\dagger \psi_j^\dagger \psi_k \psi_l \right) \end{aligned} \quad (16)$$

where k_1, k_2, k'_1, k'_2 are constrained by momentum conservation, and i, j, k and l refer to the various bands, and (a, b, c, d) are either all the same, same in pairs or all different in the above sum. Now, we are only interested in the two bands (for a given \bar{X} -point) which lie in the bulk band gap and are closer to the saddle points in energy. In particular, we shall concentrate on the positive energy bands lying closer to the saddle points for each of the \bar{X} points, in which case we can drop all the terms from the above equations except those involving ψ_2 and ψ_6 , the relevant bands in our case. We then have $c_{\uparrow 1} = u_{\uparrow 1} \psi_2$, $c_{\downarrow 1} = u_{\downarrow 1} \psi_2$, $c_{\uparrow 2} = u_{\uparrow 2} \psi_2$ and $c_{\downarrow 2} = u_{\downarrow 2} \psi_2$, and likewise for ψ_6 with the valleys 3 and 4, suppressing the contributions from the other bands. Considering only the contributions from the two lower positive energy bands (corresponding to the two \bar{X} points) which are degenerate, the above Eq. 16 can be

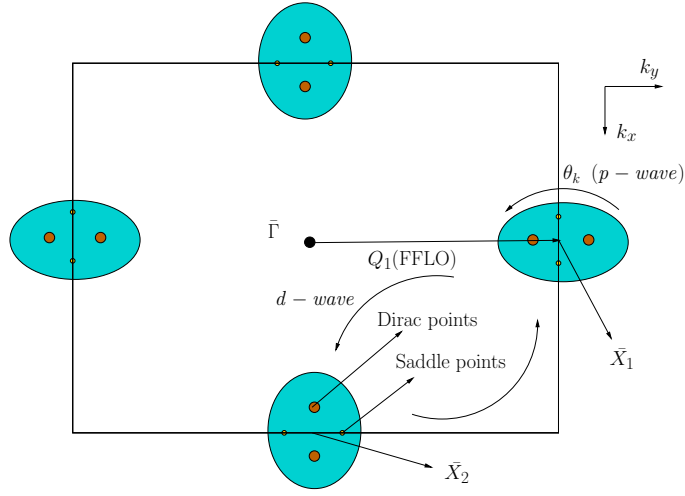


Figure 6. A schematic representation of the (001) surface with two Dirac points and saddle points each at the \bar{X}_1 and \bar{X}_2 points. The FFLO wave vector connecting the \bar{X}_1 point to the origin $\bar{\Gamma}$ is represented by Q_1 . In our analysis, we obtain a phase factor of $\exp[i(\theta_k - \theta_{k'})]$, with respect to the \bar{X} points, associated with the effective interactions in the band picture, while the relative phases of the order parameter between the patches \bar{X}_1 and \bar{X}_2 is π (*d-wave*) (with respect to the $\bar{\Gamma}$ point). The superconducting order parameter has the form $\Delta_k = \Delta_0 \begin{pmatrix} 1 \\ -1 \end{pmatrix}_{\bar{X}} \otimes \exp[i\theta_k]$. We have considered a situation where the Fermi surface of a patch encloses both the Van-Hove points. Electrons anywhere in the patch experience an enhanced density of states due to the proximity of one or more Van-Hove points.

rewritten as

$$\begin{aligned}
 H_I = & \sum_i \sum_{\sigma, \sigma'} \frac{1}{2} h_4^{\sigma\sigma'} \psi_i^\dagger \psi_i^\dagger \psi_i \psi_i \\
 & + \sum_{i \neq j} \sum_{\sigma, \sigma'} \frac{1}{2} (h_1^{\sigma\sigma'} \psi_i^\dagger \psi_j^\dagger \psi_i \psi_j \\
 & + h_2^{\sigma\sigma'} \psi_i^\dagger \psi_j^\dagger \psi_j \psi_i + h_3^{\sigma\sigma'} \psi_i^\dagger \psi_i^\dagger \psi_j \psi_j)
 \end{aligned} \tag{17}$$

where the sum is over the two low-energy bands only, and $h_1^{\sigma\sigma'} = \sum_{a,b,c,d} U_1^{\sigma\sigma'} u_{\sigma ai}^*(k'_1) u_{\sigma' bj}^*(k'_2) u_{\sigma' ci}(k_1) u_{\sigma dj}(k_2)$ (where one of the low-energy bands denoted by i has nonzero components for valleys (a, c) and the other one denoted by j for valleys (b, d)), and this gives us the corresponding coupling h_1 used in the low-energy theory in Eq.(3) of the main text, when scaled with respect to the number of such combinations of valleys. The rest of the couplings h_2 , h_3 and h_4 can be similarly defined in terms of the interactions in the valley-spin picture and the form factors for the basis transformation. Thus, there are four kinds of allowed scattering terms between electrons belonging to the two bands under consideration. These correspond to exchange processes between electrons on the two different bands (h_1), Coulomb interaction between electrons on different bands (h_2), pair hopping between the two bands (h_3) and scattering between different valleys within a band (h_4).

Susceptibilities:

The renormalization equations for the different kinds of ordering considered, in the particle-particle as well as particle-hole channel, are given as follows.

The renormalization of the test vertex corresponding to particle-hole pairing between the patches, in the $\ell = 0$ channel is given by

$$\begin{aligned}
 & \frac{\partial}{\partial y} \begin{pmatrix} \Delta_{12} \\ \Delta_{21} \end{pmatrix} = \\
 & - 2d_1(y) \begin{pmatrix} h_2^0 - h_1^0 - h_1^1 & -h_3^1 \\ -h_3^1 & h_2^0 - h_1^0 - h_1^1 \end{pmatrix} \begin{pmatrix} \Delta_{12} \\ \Delta_{21} \end{pmatrix}
 \end{aligned} \tag{18}$$

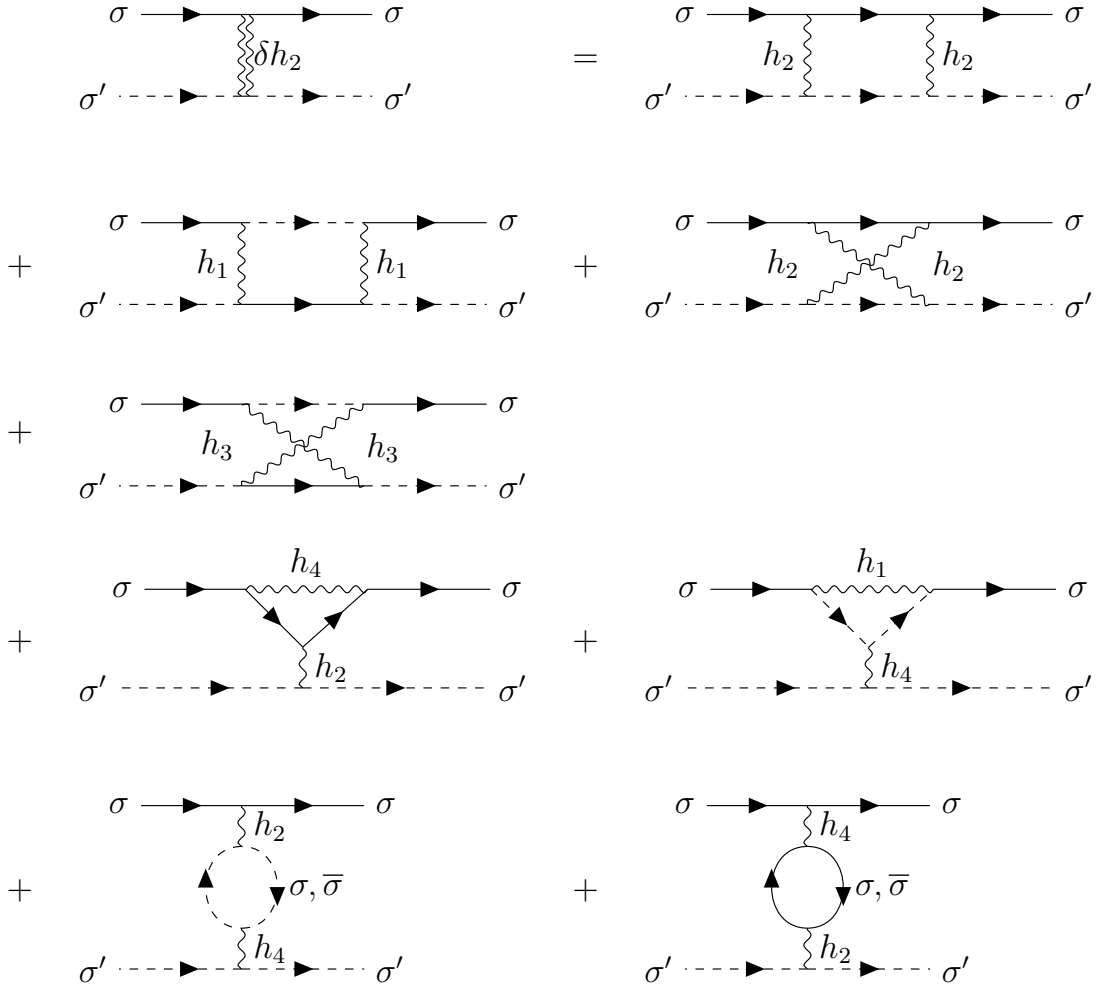


Figure 7. Diagrams for one-loop renormalization of the coupling h_2 . The diagrams for h_1 , h_3 and h_4 are similarly obtained.

and in the $\ell = 1$ channel, by

$$\frac{\partial}{\partial y} \begin{pmatrix} \Delta_{12} \\ \Delta_{21} \end{pmatrix} = -2d_1(y) \begin{pmatrix} h_2^1 & h_3^1 \\ h_1^1 & h_2^1 \end{pmatrix} \begin{pmatrix} \Delta_{12} \\ \Delta_{21} \end{pmatrix} \quad (19)$$

The renormalization of the test vertex corresponding to particle-particle pairing between the patches, in the $\ell = 0$ channel, is given by

$$\frac{\partial}{\partial y} \begin{pmatrix} \Delta_{12} \\ \Delta_{21} \end{pmatrix} = 2d_3(y) \begin{pmatrix} h_2^0 & h_1^0 \\ h_1^0 & h_2^0 \end{pmatrix} \begin{pmatrix} \Delta_{12} \\ \Delta_{21} \end{pmatrix} \quad (20)$$

and in the $\ell = 1$ channel, by

$$\frac{\partial}{\partial y} \begin{pmatrix} \Delta_{12} \\ \Delta_{21} \end{pmatrix} = 2d_3(y) \begin{pmatrix} h_2^1 & h_1^1 \\ h_1^1 & h_2^1 \end{pmatrix} \begin{pmatrix} \Delta_{12} \\ \Delta_{21} \end{pmatrix} \quad (21)$$

The renormalization of the test vertex corresponding to particle-hole pairing on a patch, in the $\ell = 0$ channel, is given by

$$\begin{aligned} \frac{\partial}{\partial y} \begin{pmatrix} \Delta_1 \\ \Delta_2 \end{pmatrix} = \\ -2d_2(y) \begin{pmatrix} -h_4^1 & h_1^0 - h_2^0 - h_2^1 \\ h_1^0 - h_2^0 - h_2^1 & -h_4^1 \end{pmatrix} \begin{pmatrix} \Delta_1 \\ \Delta_2 \end{pmatrix} \end{aligned} \quad (22)$$

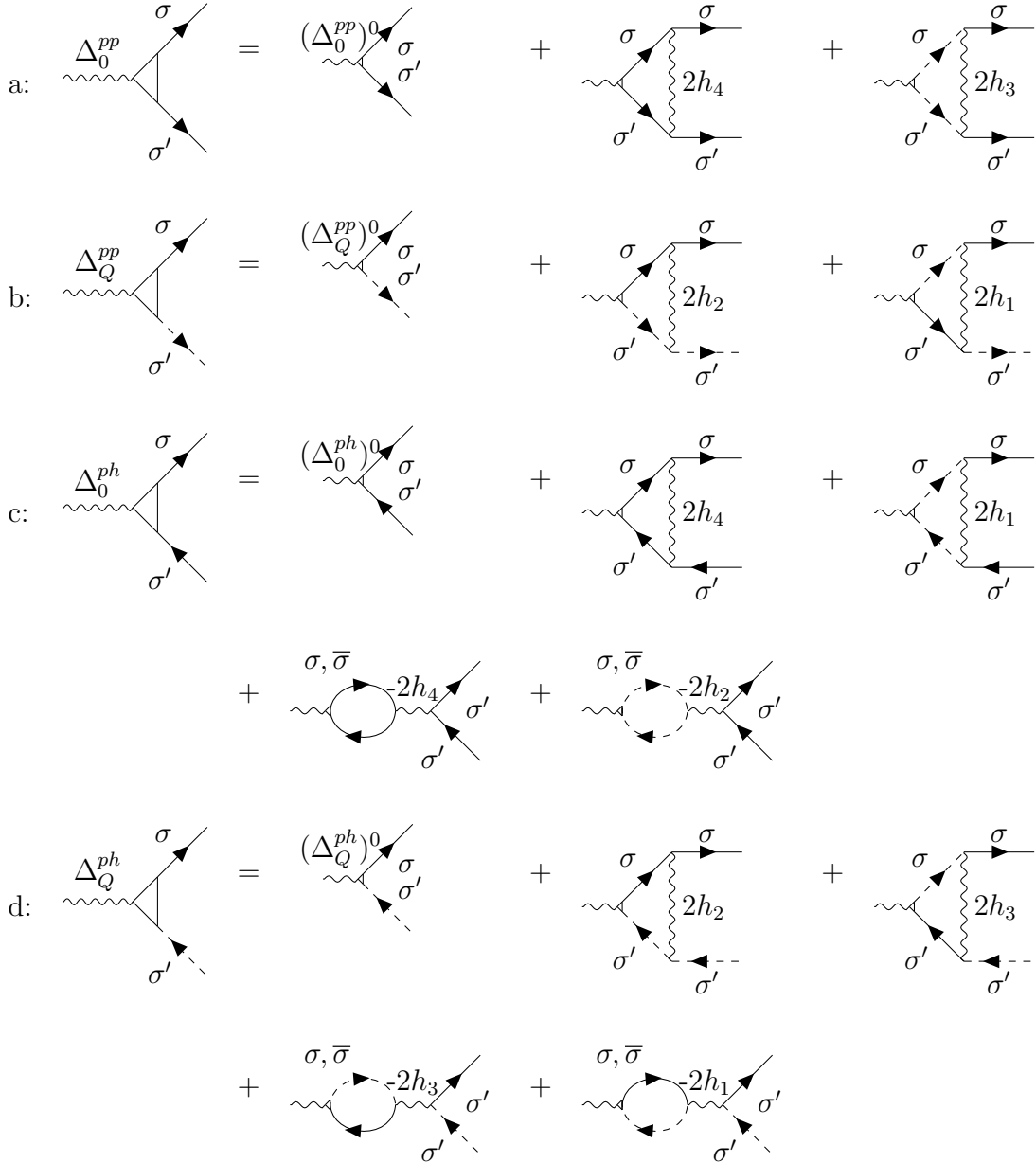


Figure 8. Test vertex renormalization corresponding to (a) particle-particle pairing on the patch, (b) particle-particle pairing between patches, (c) particle-hole pairing on the patch and (d) particle-hole pairing between patches, where Q refers to the nesting vector between the patches \bar{X}_1 and \bar{X}_2 in two dimensions.

and in the $\ell = 1$ channel, is given by

$$\frac{\partial}{\partial y} \begin{pmatrix} \Delta_1 \\ \Delta_2 \end{pmatrix} = -2d_2(y) \begin{pmatrix} h_4^1 & h_1^1 \\ h_1^1 & h_4^1 \end{pmatrix} \begin{pmatrix} \Delta_1 \\ \Delta_2 \end{pmatrix} \quad (23)$$

The diagrams corresponding to the renormalization of the different kinds of pairing vertices are shown in Fig. 8. The most negative eigenvalue for Cooper pairing on the patch is given by $2(-h_3^1 + h_4^1)$ which corresponds to the eigenvector $\frac{1}{\sqrt{2}} \begin{pmatrix} -1 & 1 \end{pmatrix}$, competing with those for CDW and SDW order, given by $-2(h_3^1 - h_1^0 - h_1^1 + h_2^0)d_1(y)$ (corresponding to the eigenvector $\frac{1}{\sqrt{2}} \begin{pmatrix} -1 & 1 \end{pmatrix}$) and $-2(h_3^1 + h_2^1)d_1(y)$ (corresponding to the eigenvector $\frac{1}{\sqrt{2}} \begin{pmatrix} 1 & 1 \end{pmatrix}$) respectively. This is followed by particle-hole pairing on a patch in the $\ell=0$ channel, with the more negative eigenvalue given by $-2(-h_4^1 - (h_1^0 - h_2^0 - h_2^1))d_2(y)$ (corresponding to the eigenvector $\frac{1}{\sqrt{2}} \begin{pmatrix} -1 & 1 \end{pmatrix}$). Thus, the dominant instability of our system, namely p -wave superconductivity, appears in the $\ell = 1$ channel.

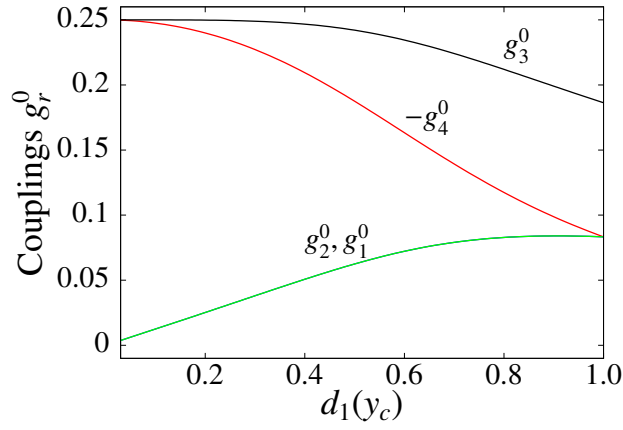


Figure 9. The fixed point values for g_r^0 as a function of $d_1(y_c)$ for the case where the $\ell=0$ components of all the couplings dominate initially. Note that the fixed point values g_2^0 and g_1^0 turn out to be identical.

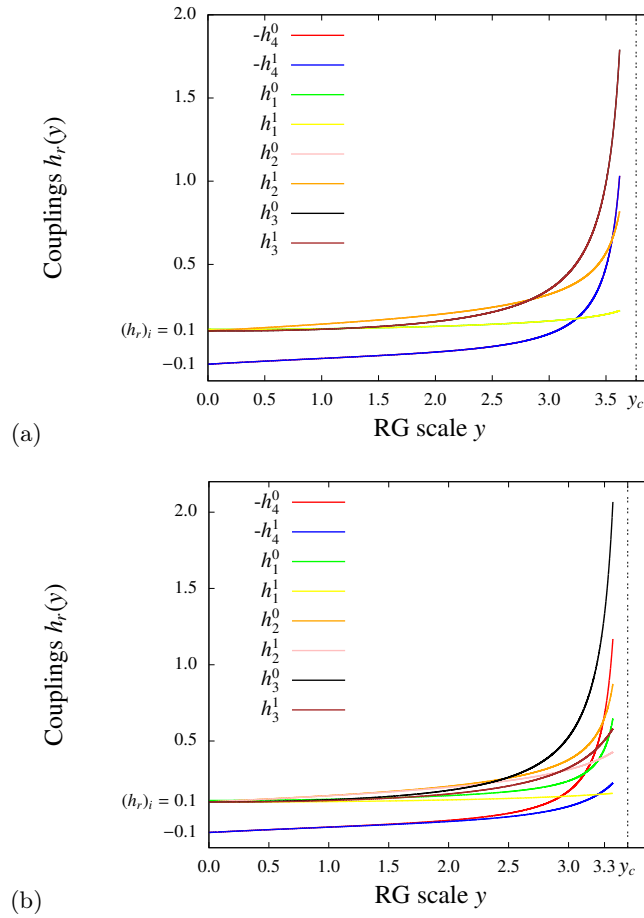


Figure 10. (a) Flow of the couplings with the RG scale y , with an initial splitting in the different scattering channels r . Here we have chosen the initial value of h_1 to be greater than all the other h_r by 10%, i.e. $\frac{|h_1^\ell - h_r^\ell|}{|h_r^\ell|} = 0.1 (r \neq 1)$ for $\ell = 0, 1$, where $(h_r^\ell)_{initial} = 0.1$ for $r \neq 1$. The resulting order of the couplings at the fixed-point y_c is identical to the case where all the couplings are chosen to be degenerate initially (see Fig.2 in main text). This illustrates that our RG flows are insensitive to the initial order of the couplings in different scattering channels $r = 1 - 4$, as long as $h_r^0 = h_r^1$ for all r . Here, the critical point $y_c \approx 3.8$.

(b) Flow of the couplings with the RG scale y , with $h_1^0 > h_1^1$ by 10% initially, i.e. $\frac{|h_1^0 - h_1^1|}{|h_1^1|} = 0.1$, where $(h_r^0)_{initial} = 0.1$ for $r \neq 1$ and $(h_r^1)_{initial} = 0.1$ for all r . This changes the order of the couplings at the fixed point drastically, and the couplings h_3^0 and $(-h_4^0)$ now dominate near the fixed point of RG flow. Here, the critical point $y_c \approx 3.5$.

Fixed point values of couplings as a function of $d_1(y_c)$:

As discussed in the main text, the different couplings $h_r^\ell(y)$ have an asymptotic form $\frac{g_r^\ell}{y_c - y}$ near the critical point y_c of the RG flow. In order to determine the behavior of the fixed point values g_r^ℓ for the different couplings as a function of $d_1(y_c)$, we substitute this asymptotic form into the RG equations (Eq.4-11 of the main text) to obtain the polynomial equations

$$\begin{aligned}
g_1^0 &= 2d_1(y_c)(-(g_1^0)^2 - (g_3^1)^2 - (g_1^1)^2 \\
&\quad + 2g_1^0g_2^0 + (g_3^0)^2), \\
g_1^1 &= 2d_1(y_c)(-2g_1^0g_1^1 + 2g_1^1g_2^0), \\
g_2^0 &= 2d_1(y_c)((g_2^0)^2 + (g_3^0)^2), \\
g_2^1 &= 2d_1(y_c)((g_2^1)^2 + (g_3^1)^2), \\
g_3^0 &= -4g_4^0g_3^0 + 2d_1(y_c)(4g_2^0g_3^0 - 2g_1^1g_3^1), \\
g_3^1 &= -4g_4^1g_3^1 + 2d_1(y_c)(2g_2^1g_3^1 \\
&\quad - 2g_1^0g_3^1 + 2g_2^0g_3^1), \\
g_4^0 &= -2(g_4^0)^2 - 2(g_3^0)^2, \\
g_4^1 &= -2(g_4^1)^2 - 2(g_3^1)^2.
\end{aligned} \tag{24}$$

These coupled equations are then solved with appropriate initial conditions, to determine g_r^ℓ ($\ell = 0, 1$) as a function of $d_1(y_c)$, which is the ratio of the particle-hole and particle-particle susceptibilities at the fixed point y_c . The behaviour of g_r^ℓ as a function of $d_1(y_c)$ when all the couplings are chosen to be degenerate initially, is shown in the inset in Fig.2 of the main text. The corresponding behavior when the degeneracy between the couplings in the $\ell = 0$ and $\ell = 1$ channels is lifted (such that $g_r^0 > g_r^1$ for all r) is shown in Fig. 9 (here we have only shown the behavior of the couplings g_r^0 , as the fixed-point values g_r^1 turn out to be very small in this case).

-
- [1] L. Fu, Phys. Rev. Lett. **106**, 106802 (2011).
[2] M. Z. Hasan and C. L. Kane, Rev. Mod. Phys. **82**, 3045 (2010).
[3] M. König, H. Buhmann, L. W. Molenkamp, T. Hughes, C.-X. Liu, X.-L. Qi, and S.-C. Zhang, J. Phys. Soc. Jpn. **77**, 031007 (2008).
[4] J. E. Moore, Nature(London) **464**, 194 (2010).
[5] X.-L. Qi and S.-C. Zhang, Rev. Mod. Phys. **83**, 1057 (2011).
[6] P. Dziawa, B. Kowalski, K. Dybko, R. Buczko, A. Szczerbakow, M. Szot, E. Łusakowska, T. Balasubramanian, B. M. Wojek, M. Berntsen, O. Tjernberg and T. Story, Nat. Mater. **11**, 1023 (2012).
[7] T. H. Hsieh, H. Lin, J. Liu, W. Duan, A. Bansil, and L. Fu, Nat. Commun. **3**, 982 (2012).
[8] Y. Tanaka, Z. Ren, T. Sato, K. Nakayama, S. Souma, T. Takahashi, K. Segawa, and Y. Ando, Nature Phys. **8**, 800 (2012).
[9] S.-Y. Xu, C. Liu, N. Alidoust, M. Neupane, D. Qian, I. Belopolski, J. Denlinger, Y. Wang, H. Lin, L. Wray, *et al.*, Nat. Commun. **3**, 1192 (2012).
[10] H. Yao and F. Yang, Phys. Rev. B **92**, 035132 (2015).
[11] I. Dzyaloshinskii, JETP Lett. **46**, 118 (1987).
[12] H. Schulz, Europhys. Lett. **4**, 609 (1987).
[13] P. Lederer, G. Montambaux, and D. Poilblanc, J. Phys. **48**, 1613 (1987).
[14] D. Yudin, D. Hirschmeier, H. Hafermann, O. Eriksson, A. I. Lichtenstein, and M. I. Katsnelson, Phys. Rev. Lett. **112**, 070403 (2014).
[15] R. Nandkishore, R. Thomale, and A. V. Chubukov, Phys. Rev. B **89**, 144501 (2014).
[16] V. P. Mineev, K. Samokhin, and L. Landau, *Introduction to unconventional superconductivity* (CRC Press, 1999).
[17] M. R. Norman, Science **332**, 196 (2011).
[18] M. Sigrist and K. Ueda, Rev. Mod. Phys. **63**, 239 (1991).
[19] N. Furukawa, T. Rice, and M. Salmhofer, Phys. Rev. Lett. **81**, 3195 (1998).
[20] R. Nandkishore, L. Levitov, and A. Chubukov, Nature Phys. **8**, 158 (2012).
[21] J.-Q. Huang, C.-H. Hsu, H. Lin, D.-X. Yao, and W.-F. Tsai, Phys. Rev. B **93**, 155108 (2016).
[22] J. Yuan and C. Honerkamp, arXiv:1504.04536 (2015).
[23] O. Vafeek and A. V. Chubukov, Physical Review Letters **118**, 087003 (2017).
[24] P. Fulde and R. A. Ferrell, Phys. Rev. **135**, A550 (1964).
[25] A. Larkin and Y. N. Ovchinnikov, Zh. Eksp. Teor. Fiz. **47**, 1136 (1964).
[26] R. Balian and N. R. Werthamer, Phys. Rev. **131**, 1553 (1963).
[27] A. P. Mackenzie and Y. Maeno, Rev. Mod. Phys. **75**, 657 (2003).
[28] P. W. Anderson, J. Phys. Chem. Solids **11**, 26 (1959).
[29] C. Zhang, S. Tewari, R. M. Lutchyn, and S. D. Sarma, Phys. Rev. Lett. **101**, 160401 (2008).
[30] K. Michaeli and L. Fu, Phys. Rev. Lett. **109**, 187003 (2012).
[31] Y. Nagai, Physical Review B **91**, 060502 (2015).

- [32] A. P. Mackenzie, R. K. W. Haselwimmer, A. W. Tyler, G. G. Lonzarich, Y. Mori, S. Nishizaki, and Y. Maeno, *Phys. Rev. Lett.* **80**, 161 (1998).
- [33] Q. L. He, L. Pan, A. L. Stern, E. C. Burks, X. Che, G. Yin, J. Wang, B. Lian, Q. Zhou, E. S. Choi, *et al.*, *Science* **357**, 294 (2017).
- [34] K. Kubo, *J. Phys. Soc. Jpn.* **77**, 043702 (2008).
- [35] Y.-T. Hsu, A. Vaezi, M. H. Fischer, and E.-A. Kim, *Nat. Commun.* **8**, 14985 (2017).
- [36] G. Y. Cho, J. H. Bardarson, Y.-M. Lu, and J. E. Moore, *Phys. Rev. B* **86**, 214514 (2012).
- [37] G. Bednik, A. Zyuzin, and A. Burkov, *Phys. Rev. B* **92**, 035153 (2015).
- [38] H. Wei, S.-P. Chao, and V. Aji, *Phys. Rev. B* **89**, 014506 (2014).
- [39] T. Zhou, Y. Gao, and Z. Wang, *Phys. Rev. B* **93**, 094517 (2016).
- [40] J. Liu, W. Duan, and L. Fu, *Phys. Rev. B* **88**, 241303 (2013).
- [41] See supplemental material.
- [42] Sarbajaya Kundu and Vikram Tripathi, *arXiv:1709.02322* (2017).
- [43] S. Das, L. Aggarwal, S. Roychowdhury, M. Aslam, S. Gayen, K. Biswas, and G. Sheet, *Appl. Phys. Lett.* **109**, 132601 (2016).
- [44] G. Mazur, K. Dybko, A. Szczerbakow, M. Zgierski, E. Lusakowska, S. Kret, J. Korczak, T. Story, M. Sawicki, and T. Dietl, *arXiv:1709.04000* (2017).
- [45] C.-K. Chiu, Y.-H. Chan, X. Li, Y. Nohara, and A. P. Schnyder, *Phys. Rev. B* **95**, 035151 (2017).
- [46] S.-Y. Xu, C. Liu, I. Belopolski, S. K. Kushwaha, R. Sankar, J. W. Krizan, T.-R. Chang, C. M. Polley, J. Adell, T. Balasubramanian, K. Miyamoto, N. Alidoust, G. Bian, M. Neupane, H.-T. Jeng, C.-Y. Huang, W.-F. Tsai, T. Okuda, A. Bansil, F. C. Chou, R. J. Cava, H. Lin, and M. Z. Hasan, *Phys. Rev. B* **92**, 075115 (2015).